Wiley Analytical Science

The Current State of Reconstruction Technologies for 3D X-ray Microscopy including Algorithmic Innovation for AI-based Recovery

April 26, 10:00am - 11:00am EDT

Many properties can only be fully understood in 3D, such as porosity and tortuosity in porous materials, network connection maps in neuroscience, or mechanical properties in 3D additively manufactured structures. X-ray microscopy provides a unique method to image samples non-destructively in 3D across a wide range of materials and life sciences.

Watch this session during the WAS Virtual Conference:

Nicolas Guenichault, Ph.D.

Dr. Stephen T. Kelly, Ph.D.

Register Now

This talk is sponsored by ZEISS

ADVANCED OPTICAL MATERIALS
www.advopticalmat.de

Reducing Efficiency Roll-Off in Multi-Resonant Thermally Activated Delayed Fluorescent OLEDs through Modulation of the Energy of the T_2 State

*Tao Wang, Abhishek Kumar Gupta, David B. Cordes, Alexandra M. Z. Slawin, and Eli Zysman-Colman**

The S_1 state and high-lying triplet excited states (ΔE_{S1Tn}) offer insight into clarifying the mechanism of efficiency roll-off of organic light-emitting diodes (OLEDs). However, experimental detection of the ΔE_{S1Tn} is challenging due to Kasha's rule. Here, two emitters, PhCz-O-DiKTa and PhCz-DiKTa, showing multi-resonant thermally activated delayed fluorescence (MR-TADF) are reported. By modulating the conjugation between the MR-TADF DiKTa emissive center and donor substituent, emission directly from the T_2 state is for the first time observed in MR-TADF emitters. Single crystal and reduced density gradient analyses reveal the origin of the reduced observed concentration-quenching results from weak CH···π and slipped π···π stacking interactions, which suppress nonradiative transitions. Theoretical and photophysical investigations reveal that the ΔE_{S1T2} difference influences the reverse intersystem crossing rate. The OLEDs employing PhCz-O-DiKTa and PhCz-DiKTa as emitters show maximum external quantum efficiencies (EQE_{max}) of over 20%, but very different efficiency roll-off behavior (54.5% vs 13.6% at 100 cd m^{-2}). Thus, this design provides a possible solution to mitigating device efficiency roll-off by designing MR-TADF emitters with degenerate S_1 and T_2 states.

1. Introduction

Organic light-emitting diodes (OLEDs) are surging in use across multiple markets such as those of wearable electronics, smartphones, flat displays, and solid-state lighting. This is largely driven by their numerous promising advantages compared to conventional liquid crystal displays (LCDs) such as lower cost, greater flexibility, better picture quality, and fast response time.[1] Fabrication of high-performance OLEDs is paramount to the success of these applications. Fluorescent OLEDs can only convert 25% of singlet excitons into emission, with the loss of 75% triplet excitons as heat.[2] In the past decade, thermally activated delayed fluorescence (TADF) materials have emerged as emitters for the third-generation OLED, able to harvest 100% of excitons to generate light, at comparable exciton utilization efficiencies to phosphorescent OLEDs. Generally, TADF emitters are based on a strongly twisted donor–acceptor (D–A) design motif to electronically separate the highest occupied molecular orbital (HOMO) and lowest unoccupied molecular orbital (LUMO) that results in a small energy gap between S_1 and T_1 states (ΔE_{S1T1}).[3–5] However, a relatively large nuclear reorganization and charge-transfer (CT) transition in the excited state unavoidably produces a broad emission band, reflected by a large full width at half maximum (FWHM) of around 100 nm.[6] These undesired properties in D–A TADF emitters restrict their practical application in high-resolution displays where the color point requirements demanded by industry are difficult to obtain using materials showing broad emission.

At present, commercialized high-resolution OLED displays mainly employ a color filter or microcavity to reach the color purity required by broadcasting standards, which is inevitably accompanied by losses in device efficiency and energy utilization.[7] Therefore, it would be of great utility to devise an emitter showing narrowband emission. Recently, Hatakeyama et al. introduced a subclass of TADF emitters coined multi-resonant TADF (MR-TADF), that shows the desired narrowband emission. This is due to their rigid polyaromatic hydrocarbon (PAH) framework,[8] where the rigid molecular skeleton and the short-range CT (SRCT) nature of the emissive singlet excited state enable simultaneously narrowband emission and small ΔE_{S1T1}. In this design, the electron densities of the HOMO and LUMO are localized on the adjacent atoms. Typically, boron/nitrogen (B/N) doped PAHs have emerged as the dominant design. For example, Hatakeyama and co-workers designed a B/N-doped MR-TADF compound, ***ν*-DABNA**, that shows very narrowband emission (FWHM of 18 nm) at a photoluminescence (PL) maximum (λ_{PL}) of 467 nm, with a PL quantum yield (Φ_{PL}) of 90%, and where the device's maximum external quantum efficiency

T. Wang, A. K. Gupta, D. B. Cordes, A. M. Z. Slawin, E. Zysman-Colman
Organic Semiconductor Centre
EaStCHEM School of Chemistry
University of St Andrews
St Andrews KY16 9ST, UK
E-mail: eli.zysman-colman@st-andrews.ac.uk

The ORCID identification number(s) for the author(s) of this article can be found under https://doi.org/10.1002/adom.202300114.

DOI: 10.1002/adom.202300114

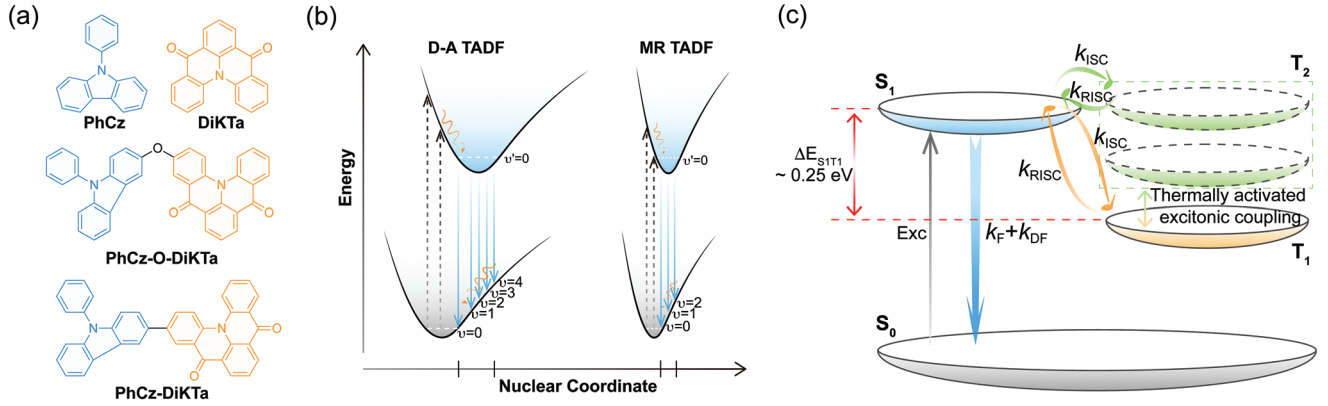

Figure 1. a) Chemical structures of MR-TADF building blocks (**PhCz** and **DiKTa**) and the emitters (**PhCz-O-DiKTa** and **PhCz-DiKTa**) investigated in this work. b) Schematic illustration of simplified Jablonski diagrams outlining the origin of the narrowband emission in MR-TADF emitters. c) Schematic illustration of T_2-regulated RISC in MR-TADF emitters; Exc: Excitation; F: Fluorescence; DF: Delayed fluorescence.

(EQE_{max}) was an impressive 34.4%.[9] A hyperfluorescence (HF) strategy has been extensively employed to mitigate efficiency roll-off in the device, wherein generally a TADF emitter serves as the assistant dopant to efficiently harvest excitons and then these are efficiently transferred to the terminal emitter, a compound showing narrowband emission and with a fast radiative rate constant, k_r.[10] Benefitting from these pioneering works, Lee and co-workers reported an HF device that showed an EQE_{max} of 33.5% and a long operational device lifetime (LT_{50}, 50% of initial luminance) of 9500 h at 100 cd m^{-2} by employing ***ν*-DABNA** as the terminal emitter and a triazine derivative **PPCzTrz** as the assistant dopant;[11] the device with only ***ν*-DABNA** as the emitter was much less stable (LT_{50} = 31 h).[9] A similarly themed report by Adachi and co-workers documented an HF device using ***ν*-DABNA** as the terminal emitter with an EQE_{max} of 41% and an LT_{50} > 10 000 h.[12] Besides HF, other strategies have been explored to improve the performance of MR-TADF OLEDs.[13–18] For instance, Yang and co-workers proposed an effective strategy for mitigating aggregation-caused quenching (ACQ) by introducing sterically bulky groups onto a B/N-doped emitter.[13]

Carbonyl (C=O)/N-doped PAHs are a second family of MR-TADF emitters.[19–24] Initial studies by Yuan et al. and us using **DiKTa** (**Figure 1**a) derivatives documented the potential of this design;[21,25] however, the devices typically suffered from significant efficiency roll-off (>30%) at 100 cd m^{-2} and low maximum luminance ($L_{max} \leq 13\,000$ cd m^{-2}). Recently, we demonstrated that by decorating **DiKTa** with various donors, the OLEDs showed an improved EQE_{max} and reduced efficiency roll-off compared to the device with the parent emitter;[26] however, this improvement in efficiency roll-off was not present beyond 100 cd m^{-2}. Similarly, Zhang and co-workers reported three C=O/N-doped PAHs, **QAD-Cz**, **QAD-2Cz**, and **QAD-mTDPA**.[27] Although having very similar molecular structures and near unity Φ_{PL}, there is a stark dichotomy in the observed efficiency roll-off at 100 cd m^{-2} (**QAD-Cz**: 73.4%, **QAD-2Cz**: 12.5%, and **QAD-mTDPA**: 51.0%). These results provide insight that a high-lying triplet excited state (T_n) is likely responsible for the differences in reverse intersystem crossing (RISC) rate constants, k_{RISC}, and thus the different efficiency roll-off profiles. Improved MR-TADF design can be realized if we were above to experimentally determine the energy of these close-lying triplet states to the S_1 state. The employment of transient absorption spectroscopy can be used to detect the existence of T_n states,[28] but it lacks the capability of quantifying the energy of these states. Very recently, transient electron paramagnetic resonance spectroscopy (EPR) was employed by Evans and co-workers to reveal that multiple triplet excited states aid to mediate delayed fluorescence.[29] In our previous work, we utilized transient EPR to distinguish the T_2 and T_1 states of the anthracene derivative **DPAAnCN** and revealed that exciton harvesting proceeded by a hybridized local and charge-transfer (HLCT) fluorescence mechanism. Despite these advances, it remains challenging to map out the triplet-state landscape.

We recently demonstrated using time-resolved PL spectroscopy that higher-lying triplet states could be observed in multiple-phosphorescence emitters.[30,31] Capitalizing on this design paradigm, here we utilize conjugation modulation as a tool to brighten the T_2 state of MR-TADF emitters. We report two **DiKTa** derivatives **PhCz-O-DiKTa** and **PhCz-DiKTa** (Figure 1a), and explore the impact of conjugation from the decorated donor moiety on the efficiency roll-off of the OLED (Figure 1b); in the conceived emitter design the degree of conjugation between 9-phenyl-9*H*-carbazole (**PhCz**) and **DiKTa** is employed to regulate the vibronic coupling between two triplet excited states and activate emission from the T_2 state; **PhCz** acts as a perturbator of the energy of the T_2 state to tune k_{RISC} (Figure 1c). The Φ_{PL} values as a function of doping level reveal that both emitters are reasonably resistant to concentration quenching. The existence of the T_2 state was demonstrated by time-resolved PL measurements and further confirmed by the observable T_2 afterglows. The OLED devices employing **PhCz-O-DiKTa** and **PhCz-DiKTa** as emitters indicate 100% exciton utilization assuming a 25% out-coupling efficiency. Similar EQE_{max} (**PhCz-O-DiKTa**: 20%; **PhCz-DiKTa**: 22%) values were obtained; however, there is a stark contrast in efficiency roll-off at 100 cd m^{-2} (**PhCz-O-DiKTa** at 54.5% and **PhCz-DiKTa** at 13.6%).

2. Results and Discussion

2.1. Synthesis and Structural Characterization

PhCz-O-DiKTa and **PhCz-DiKTa** were synthesized via Ullmann condensation and Suzuki–Miyaura coupling reactions using

PhCz and **DiKTa** as building blocks. The synthetic routes are outlined in Scheme S1, Supporting Information. All samples were purified via silica column chromatography followed by temperature-gradient vacuum sublimation. A combination of ^{1}H & ^{13}C nuclear magnetic resonance spectroscopy (NMR), high-resolution mass spectrometry (HRMS), melting point determination, high-performance liquid chromatography (HPLC), elemental analysis (EA), and single-crystal X-ray diffraction were used to confirm the molecular structures and assess their purity (Figures S1–S13 and Table S1, Supporting Information).

2.2. Theoretical Modeling

First, the photophysical properties of **PhCz-O-DiKTa** and **PhCz-DiKTa** were modeled using density functional theory at the PBE0/6-31G(d,p) level.[32,33] As shown in **Figure 2**a, **PhCz-O-DiKTa** and **PhCz-DiKTa** possess the LUMOs of similar energy and character, reflected by the **DiKTa**-localized density distribution. A slight energy difference between the HOMOs of the two compounds was observed, where the HOMO is localized on the **PhCz** subunit in **PhCz-O-DiKTa** but destabilized in **PhCz-DiKTa** due to the extended π-conjugation possible in this compound. Time-dependent (TD) DFT calculations within the Tamm–Dancoff approximation (TDA)[34] performed at the same level of theory predict that **PhCz-O-DiKTa** has a larger spin-orbit coupling constant between the S_1 and T_1 states at the optimized S_1 geometry than **PhCz-DiKTa** (0.43 vs 0.10 cm^{-1}) but similar oscillator strength (0.11 vs 0.12), and both exhibit a relatively large energy gap between S_1 and T_1, $\Delta E_{S1T1} > 0.4$ eV, (Figure S14a, Supporting Information), which implies that neither compound will show TADF. Calculated vertical excitations to the S_1 state predict that the character of this state in both compounds is hybridized local and CT (Figure S14b, Supporting Information). We have previously demonstrated the importance of using wavefunction-based methods to accurately model the excited state energies and ΔE_{S1T1} of MR-TADF emitters,[35,36] thus, we computed the energies of low-lying singlet and triplet excited states using spin-component scaling second-order algebraic diagrammatic construction (SCS-ADC(2)) functional with the cc-pVDZ basis set (Figure 2b).[37] The calculation data are summarized in Table S2, Supporting Information. As anticipated, a somewhat reduced ΔE_{S1T1} (≈0.25 eV) exists in both **PhCz-O-DiKTa** and **PhCz-DiKTa**. The S_1 oscillator strength of both compounds is over 0.24, reflecting a highly emissive state. The calculated distance (d_{CT}) of the S_1 state of **DiKTa** is 0.803 Å (Table S1, Supporting Information). A similar d_{CT} exists in **PhCz-O-DiKTa** (0.944 Å), but a larger value is recorded for **PhCz-DiKTa** (1.292 Å) due to the π-conjugated geometry. Nevertheless, difference density plots of the four lowest-lying excited states reveal a remarkably SRCT localized on the **DiKTa** core (Figure 2b). Such a small reorganization of the electron density in the S_1 state is expected to translate into a narrowband emission. The difference density plots for **PhCz-O-DiKTa** and **PhCz-DiKTa** are similar to that of **DiKTa** (Figure S15, Supporting Information), thus demonstrating that the incorporation of **PhCz** only causes a perturbation of the excited-state energies without remarkably influencing the nature of the low-lying excited-states. Notably, although an ΔE_{S1T1} of ≈0.25 eV has been predicted, it remains challenging to achieve fast k_{RISC} at 298 K with this energy gap as according to the Boltzmann distribution, the approximate exciton ratio between the S_1 and T_1 is 6×10^{-5}:1. Thus, to promote RISC in these compounds, a higher-lying triplet excited state T_2 of different orbital type to the S_1 state must be implicated to enable second-order coupling.[28] The calculations predict that the S_1 and T_2 states of the two emitters are dominated by SRCT and n-π^*

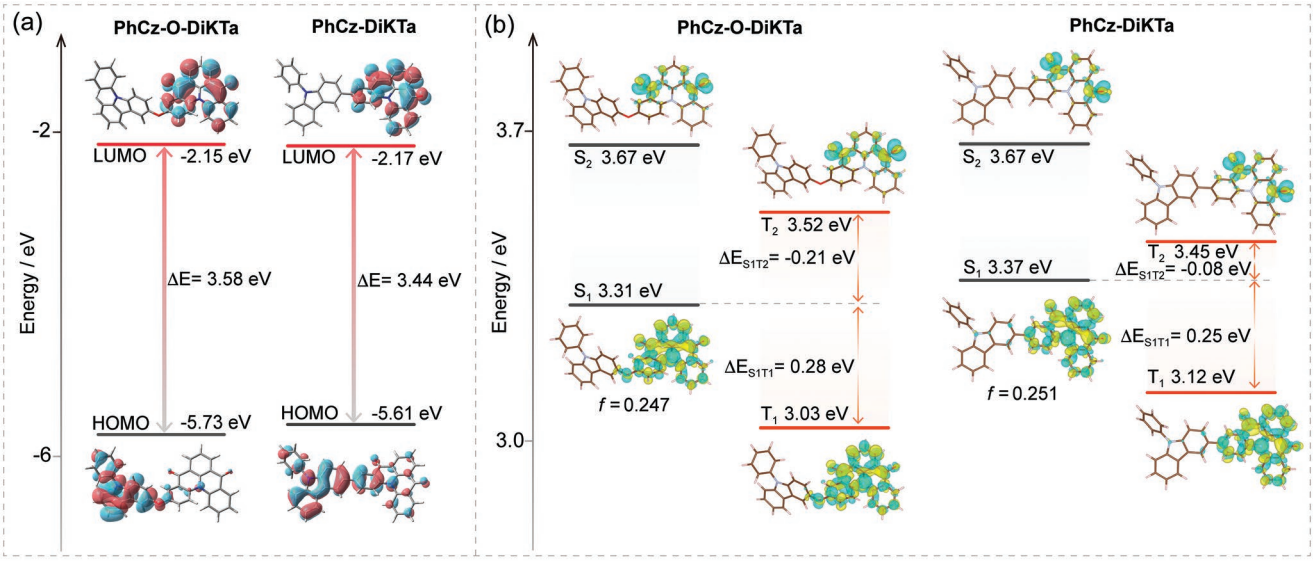

Figure 2. a) Electron density distributions and energy levels of the frontier molecular orbitals (isovalue: 0.02) calculated at the PBE0/6-31G(d,p) level. b) Different density plots (isovalue: 0.001) and excitation energy levels of excited states calculated in the gas phase at the SCS-ADC(2)/cc-pVDZ level; blue and green denote decreased and increased electron densities in the excited state compared to the ground state, respectively; *f* indicates oscillator strength.

transitions (Figure 2b), respectively. **PhCz-DiKTa** possesses a smaller ΔE_{S1T2} than that of **PhCz-O-DiKTa** (0.21 vs −0.08 eV) (Figure 2b). Therefore, we can reasonably expect that faster k_{RISC} and shorter TADF lifetime (τ_{DF}) occur in **PhCz-DiKTa** than in **PhCz-O-DiKTa** via second-order spin-vibronic coupling. As a result, it is vital to experimentally detect the T_2 energy to clarify the RISC processes.

2.3. Optoelectronic Characterization in Solution

We next investigated the optoelectronic properties in dilute solution. The energies of FMOs were inferred from the electrochemistry, where oxidation and reduction potentials (E^{ox}/E^{red}) were obtained using cyclic voltammetry (CV) and differential pulse voltammetry (DPV) in deaerated dichloromethane (DCM) with 0.1 M [^{n}Bu$_4$N]PF$_6$ as the supporting electrolyte. The electrochemical data are presented in Table S3, Supporting Information. The E^{ox}/E^{red} values of **PhCz-O-DikTa** and **PhCz-DiKTa** determined from the DPV peaks, are 1.26/−1.34 and 1.27/−1.35 V, respectively, versus SCE (**Figure 3**a), with corresponding HOMO/LUMO values of −5.60/−3.00 and −5.61/−2.99 eV, respectively. The similar FMO energies disclose the almost identical electronic configurations of the HOMO and LUMO in these two compounds. The slightly different FMO energies of **PhCz-O-DikTa** and **PhCz-DiKTa** compared to those of **DiKTa** (HOMO = −5.93 eV, LUMO = −3.11 eV)[25] result from the weak electron-donation of the **PhCz** donor with the **DiKTa** core.

UV–vis absorption spectra of the two emitters in toluene reveal a relatively intense SRCT transition at ≈450 nm (Figure 3b). Compared to **DiKTa**,[25] **PhCz-O-DiKTa** possesses a similar absorption coefficient ($\varepsilon < 1 \times 10^4$ M^{-1} cm^{-1}) around 300–400 nm, which is highly enhanced in **PhCz-DiKTa** due to the π-conjugated geometry. At 298 K, narrowband emissions were evidenced in the steady-state PL spectra of **PhCz-O-DikTa** and **PhCz-DiKTa**, with λ_{PL} at 478 and 490 nm and FWHMs of 39 and 55 nm (Figure 3b), respectively. The narrower and slightly blue-shifted emission of **PhCz-O-DiKTa** results from the π-conjugation-breaking geometry, which restricts the electronic coupling between **PhCz** and **DiKTa**. This is reflected by the larger interplanar angle between **PhCz** and **DiKTa** in **PhCz-O-DikTa** (71.07°) versus **PhCz-DiKTa** (21.95°), based on the optimized S_1 geometry (Figure S16a, Supporting Information). PL lifetimes (τ_{PL}) of **PhCz-O-DikTa** and **PhCz-DiKTa** recorded at the emission maximum in the air are 7.7 and 7 ns (Figure S17a, Supporting Information), respectively, which increase to 8.6 and 8.7 ns under N_2 (Figure S17b, Supporting Information), respectively. From Figure 3d,e, a more pronounced positive solvatochromism is observed in **PhCz-DiKTa**, which reflects the larger degree of conjugation of the **PhCz** ground and its perturbation of the SRCT state to have more long-range CT (LRCT)

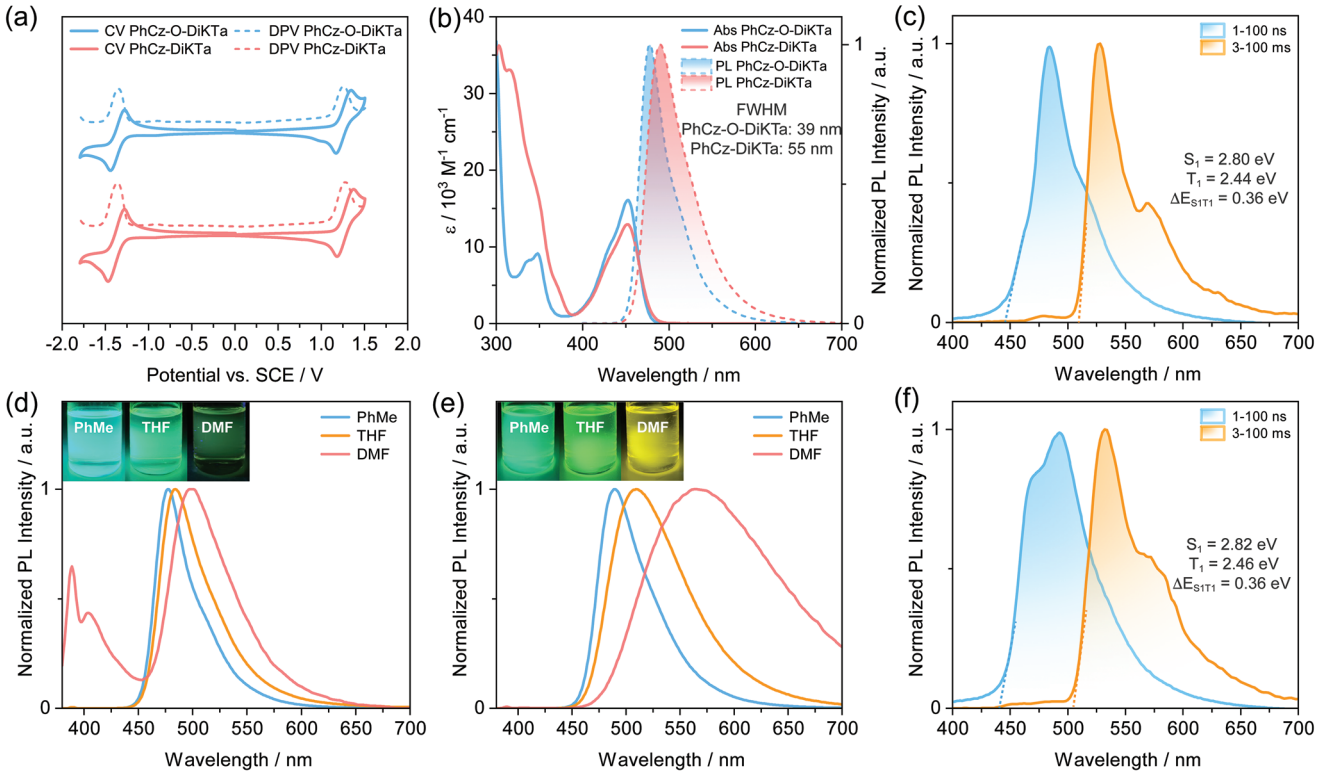

Figure 3. a) Cyclic and differential pulse voltammograms in degassed DCM with 0.1 M [^{n}Bu$_4$N]PF$_6$ as the supporting electrolyte and Fc/Fc$^+$ as the internal reference (0.46 V vs SCE).[38] b) UV–vis absorption and steady-state PL spectra recorded in aerated toluene at 298 K. Prompt (1–100 ns, λ_{exc} = 375 nm) and delayed (3–100 ms, λ_{exc} = 350 nm) PL spectra of c) **PhCz-O-DiKTa** and f) **PhCz-DiKTa** in 2-MeTHF at 77 K; concentration: 1×10^{-5} M. Solvatochromic PL study of d) **PhCz-O-DiKTa** and e) **PhCz-DiKTa** at 298 K in the air (λ_{exc} = 350 nm); inset: photos showing luminescence excited by a 365 nm UV torch.

character; this is also substantiated by a larger calculated S_1 d_{CT} (1.292 Å) compared with that of **PhCz-O-DiKTa** (d_{CT} = 0.944 Å). The emission of **PhCz-O-DiKTa** at ≈400 nm in DMF is ascribed to LE emission (Figure 3d). In degassed toluene, steady-state PL intensities of the two emitters are both enhanced compared to those recorded in aerated toluene (Figure S18, Supporting Information). Φ_{PL} values of **PhCz-O-DikTa** and **PhCz-DiKTa** in aerated toluene are 62% and 45%, which improve to 71% and 61%, respectively, demonstrating the contribution from triplet excitons (Figure S19, Supporting Information). The ΔE_{S1T1} values of **PhCz-O-DikTa** and **PhCz-DiKTa** were estimated to be 0.36 eV, from the difference in energy of the onset of prompt and delayed emission spectra in 2-methyltetrahydrofuran (2-MeTHF) glass at 77 K (Figure 3c,f). The photophysical data are summarized in Table S4, Supporting Information. The magnitude of this ΔE_{S1T1} implies that TADF is not operational in these compounds. Reminiscent of the design model (Figure 1c) and theoretical calculations (Figure 2b), the higher-energy emission band probably originates from a higher degenerate triplet excited state, here defined as the T_2 state, which is expected to be the bridge for TADF occurrence in this design.

2.4. Analysis of Intermolecular Interactions

Prior to investigating the photophysical behaviour in the solid state, we first studied the X-ray single crystal structures of **PhCz-O-DiKTa** and **PhCz-DiKTa** to elucidate what influence if any intermolecular interactions would have on the photophysics; interactions that would be present at a high doping concentration in the film state. From **Figure 4**a, **PhCz-O-DiKTa** exhibits a larger interplanar angle (83.09°) between the **PhCz** and **DiKTa** subunits than **PhCz-DiKTa** (32.02°) due to the presence of the sp^3-hybridized oxygen atom (Figure S16b, Supporting Information). As a result of the more twisted geometry, **PhCz-O-DiKTa** exhibits weaker $\pi\cdots\pi$ stacking interactions than **PhCz-DiKTa** in the dimer (Figure 4a), although they do act in a mutually supportive manner. **PhCz-O-DiKTa** packs in a head-to-tail manner, but each end of the molecule interacts with a separate neighboring molecule, leading to the formation of weakly interacting chains. The more planar **PhCz-DiKTa** also displays a head-to-tail intermolecular stacking pattern, but with both head and tail of the molecule interacting with the same neighbor, and thus strengthens molecular electronic coupling between adjacent emitter molecules, and broadens the PL. The reduced density gradient (RDG) analysis using the Multiwfn program[39] corroborates the existence of intermolecular Van de Waals interactions, as well as weakly repulsion steric interactions (Figure 4b), which are beneficial to restricting molecular motions.

2.5. Photophysical Investigations in the Solid State

We next turned our attention to the photophysical characterization in an OLED-relevant host matrix, 1,3-bis(*N*-carbazolyl)benzene (mCP) as it has a suitably high triplet energy (E_T = 3 eV).[40] The mCP matrix can also contribute to the suppression of non-radiative processes in the emitters, and host–guest interactions can also regulate triplet vibronic coupling and energies.[30,41] We first studied the steady-state PL behavior of the two emitters in mCP at various doping concentrations (Figure S20, Supporting Information). As the doping concentration increases from 1 to 10 wt%, there is only an ≈8 nm red-shift of the PL in both of **PhCz-O-DiKTa** and **PhCz-DiKTa**. This study reveals that there is very little aggregation at these doping concentrations as suggested by the absence of strong intermolecular interactions in the crystal structures. A remarkable enhancement in the Φ_{PL} values of 80% and 91% for **PhCz-O-DikTa** and **PhCz-DiKTa** in N_2, respectively, was recorded at 10 wt% doping compared to

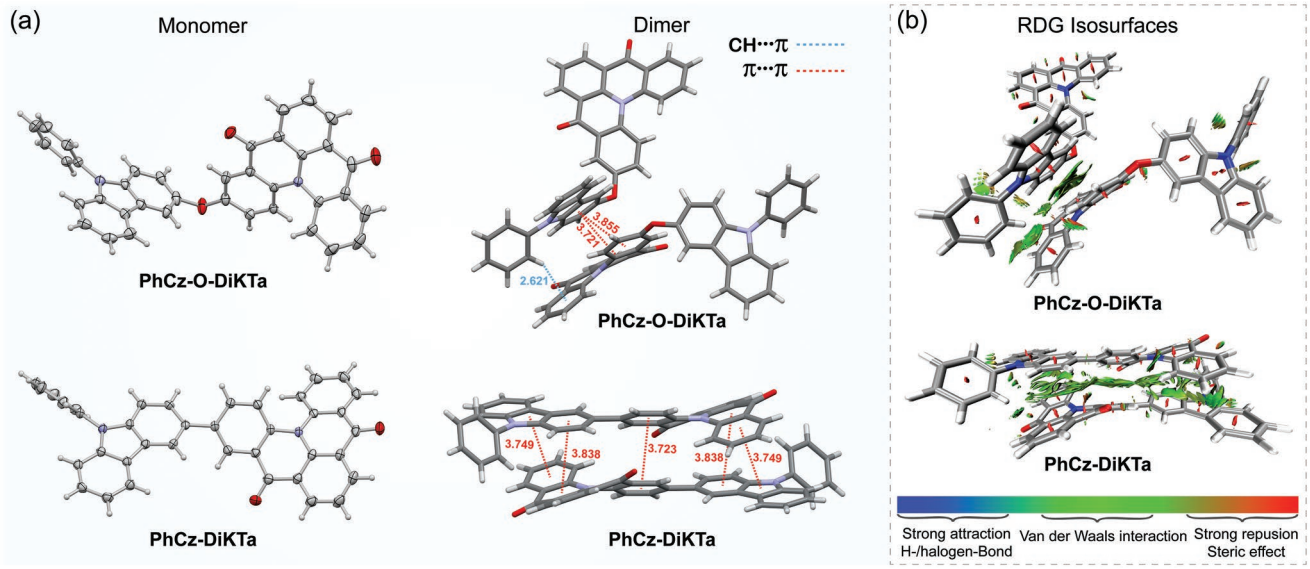

Figure 4. a) X-ray single crystal structures of **PhCz-O-DiKTa** and **PhCz-DiKTa**; ellipsoids are drawn at the 50% probability level for isolated molecules; intermolecular H···centroid and centroid···centroid distances are presented between adjacent molecules (distances in Å). b) RDG mapped with isosurfaces (isovalue: 0.5) showing intermolecular interactions based on the dimers from single crystals.

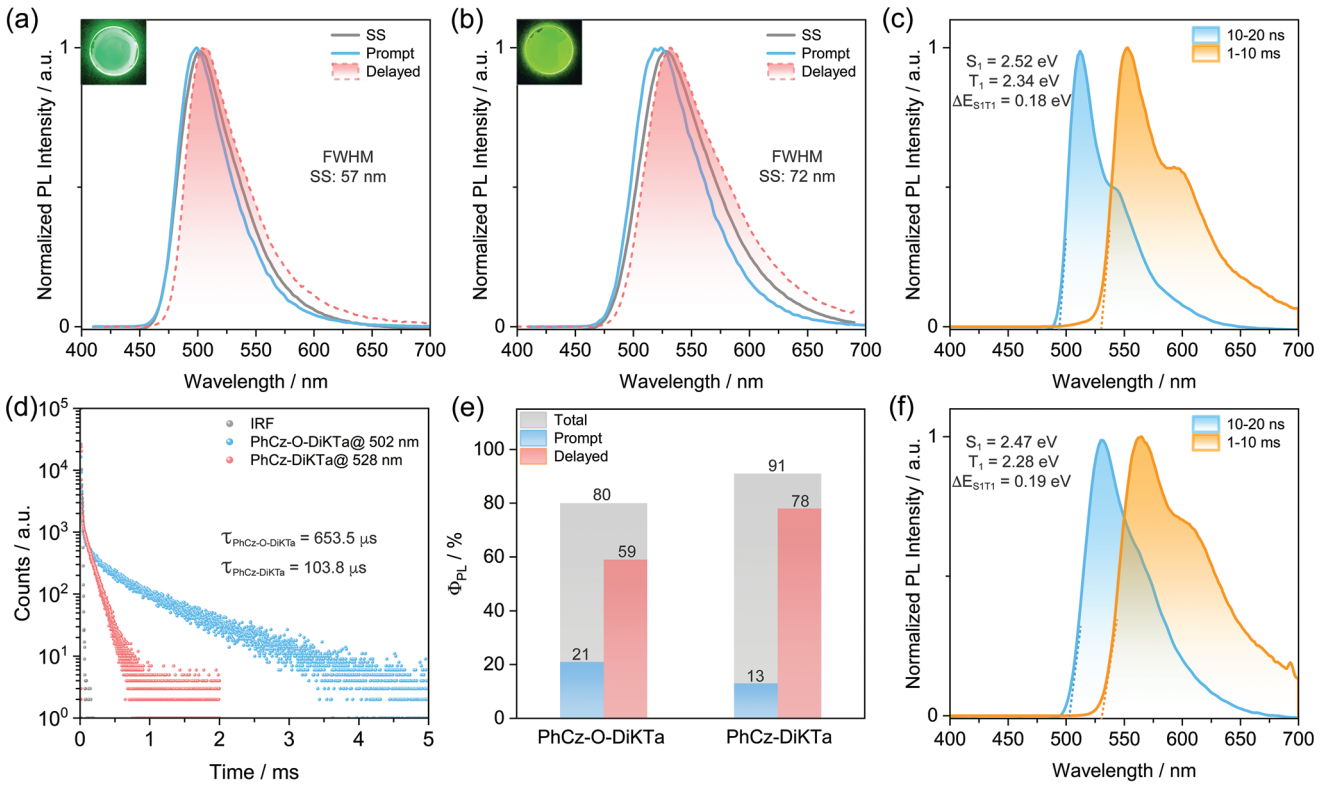

Figure 5. PL spectra of a) 10 wt% **PhCz-O-DiKTa** and b) 10 wt% **PhCz-DiKTa** in mCP at 298 K; SS: steady-state PL in the air; prompt PL in the air: 10–20 ns; delayed PL in a vacuum: 1–10 ms for **PhCz-O-DiKTa** and 0.2–2 ms for **PhCz-DiKTa**; inset: photos showing luminescence excited by 365 nm UV torch. c) Time-resolved PL decay profile in vacuum at 298 K. d) Total Φ_{PL} and corresponding contributions from prompt and delayed components. Prompt (10–20 ns, λ_{exc} = 375 nm) and delayed (1–10 ms, λ_{exc} = 350 nm) PL spectra of e) **PhCz-O-DiKTa** and f) **PhCz-DiKTa** in vacuum at 77 K.

those at 1 (Φ_{PL} < 55%) and 5 wt% (Φ_{PL} < 70%) doping (Table S5, Supporting Information). Thus, 10 wt% emitter-doped mCP films were selected for further photophysical measurements. The corresponding photophysical data are summarized in Tables S6 and S7, Supporting Information. Similar spectral profiles of the steady-state (SSPL), prompt, and delayed emissions were recorded in **PhCz-O-DiKTa** and **PhCz-DiKTa**, with the SSPL maxima, λ_{PL}, of ≈500 and ≈525 nm (**Figure 5**a,b), respectively; the FWHMs of **PhCz-O-DiKTa** and **PhCz-DiKTa** are 57 and 72 nm, respectively. The spectral FWHM broadening probably results from the enhanced electronic coupling from interactions of dimeric species in addition to host–guest interactions compared to the emission of isolated monomers (Figure 3b). Multiexponential decay kinetics were observed, with prompt fluorescence lifetimes, τ_P, for **PhCz-O-DiKTa** and **PhCz-DiKTa** of 8 and 10.1 ns (Figure S21, Supporting Information), respectively, and delayed fluorescence lifetimes, τ_{DF}, of 653.5 and 103.8 μs in vacuum (Figure 5d), respectively. Temperature-dependent transient PL decay behavior revealed that both compounds are TADF emitters (Figure S22, Supporting Information). The recorded Φ_{PL} values of **PhCz-O-DiKTa** and **PhCz-DiKTa** in the air are 56% and 73% (Table S6, Supporting Information), respectively, which improve to 80% and 91% in N_2, respectively. Based on the contribution of the delayed component to the average τ_{DF}, the calculated Φ_{DF} associated with the delayed fluorescence in N_2 is 59% and 78% for **PhCz-O-DiKTa** and **PhCz-DiKTa**, respectively (Figure 5e). The ΔE_{S1T1} values estimated from the difference in energy between the onsets of the prompt fluorescence and delayed emission are almost identical (0.18 vs 0.19 eV) (Figure 5c,f). However, the calculated k_{RISC} values of **PhCz-O-DiKTa** and **PhCz-DiKTa** are 5.44×10^3 and 6.64×10^4 s^{-1} (Table S7, Supporting Information), respectively, representing a 12-fold enhancement in the latter despite the similar ΔE_{S1T1}. However, according to Marcus electron transfer theory,[42] the k_{RISC} of **PhCz-DiKTa** should be slower than that of **PhCz-O-DiKTa** because the SOC constant of **PhCz-DiKTa** between S_1 and T_1 states is much smaller than that of **PhCz-O-DiKTa** (0.10 versus 0.43 cm^{-1}, Figure S14a, Supporting Information). Thus, a higher-lying triplet excited state T_2 probably serves as a bridge for boosting the spin vibronic coupling via second-order perturbation.

Temperature-dependent PL measurements were further performed to evidence the presence of the T_2 state. As temperature decreases from 298 to 200 K, the λ_{PL} of the steady-state PL spectrum of **PhCz-O-DiKTa** gradually red-shifts from 504 to 512 nm (**Figure 6**a), together with a remarkable enhancement in emission intensity. This excludes TADF as the origin for this spectral change as the intensity should weaken with decreasing temperature if the origin were TADF. Thus, this highly strengthened PL must originate from emission from triplet excitons. As the temperature further decreases to 77 K, the emission intensity at 512 nm diminishes accordingly, and a new concomitant T_1 emission at 540 nm emerges. Evidently, the intensity ratio between 540 and 512 nm increases due to the

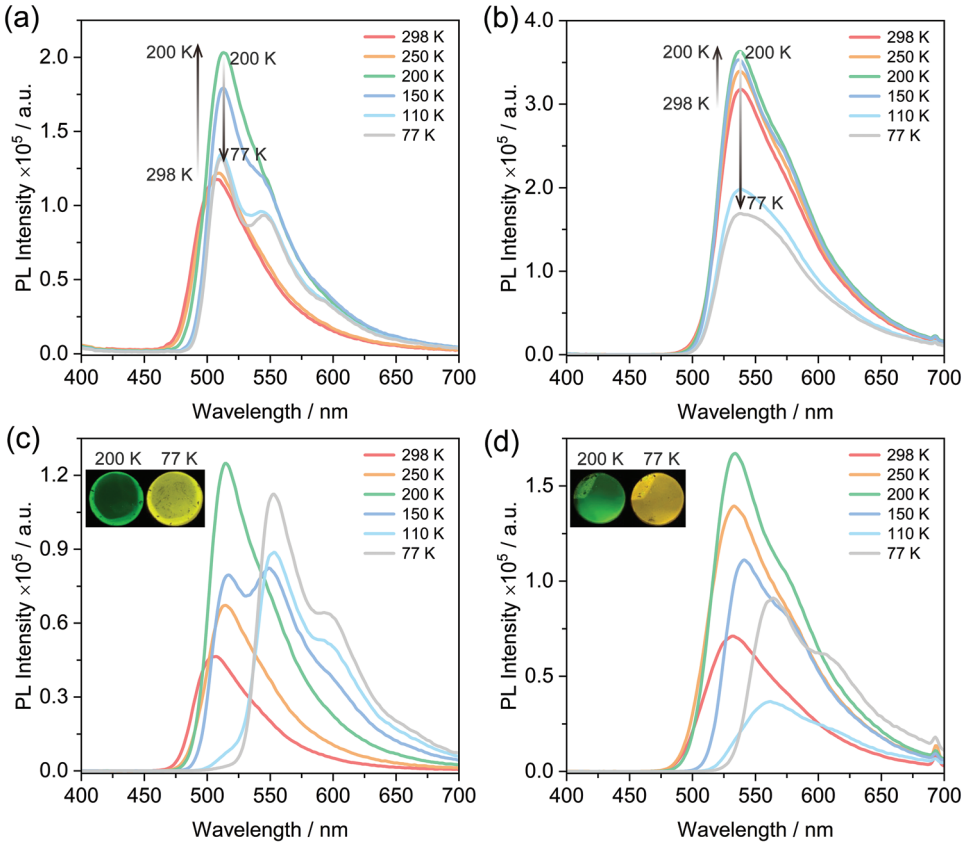

Figure 6. Temperature-dependent a,b) steady-state and c,d) time-gated PL spectra of a,c) 10 wt% **PhCz-O-DiKTa** and b,d) 10 wt% **PhCz-DiKTa** in mCP in a vacuum. Time-gated window: 1–10 ms for **PhCz-O-DiKTa** and 0.2–2 ms for **PhCz-DiKTa**; λ_{exc} = 350 nm; inset: photos showing variable afterglows at 200 K and 77 K, excited by 365 nm UV torch.

suppressed thermal activation of excitons from T_1 to T_2 states (Figure 6a). The picture of **PhCz-DiKTa** is similar as a function of temperature (Figure 6b). Next, temperature-dependent time-gated measurements were conducted to isolate the T_1 and T_2 emissions. As the temperature decreases to 200 K, compared to the TADF emission at ≈500 nm, the enhanced T_2 phosphorescence centered at 515 nm appears (as a result of the combined suppressed RISC and nonradiative transitions), and then gradually disappears. Alongside this, there is the emergence and enhancement of T_1 phosphorescence at 550 nm as temperature decreases to 77 K, which cuts off thermally activated reverse internal conversion. T_1 and T_2 phosphorescence can also be evidenced by green and yellow phosphorescence afterglows at 200 and 77 K (Figure 6c, inset), respectively. Notably, the T_2 emission recorded in mCP is blue-shifted compared to T_1 recorded in 2-MeTHF glass at 77 K, which removes the possibility that T_2 phosphorescence originates from emission from low-energy aggregates (Figure S23, Supporting Information). A similar phosphorescence evolution over temperature can be observed in **PhCz-DikTa (**Figure 6d). At 200 K, there is a strongly enhanced T_2 phosphorescence at 534 nm, while at 77 K T_1 phosphorescence dominates the time-gated PL spectrum. Similarly, two different phosphorescence afterglows were observed at 200 and 77 K (Figure 6d, inset). Normalized phosphorescence spectra of **PhCz-DiKTa** and **PhCz-O-DiKTa** gradually red-shift with decreasing temperature, reflecting the varying contributions from emissive T_2 and T_1 states (Figure S24, Supporting Information). The increasing phosphorescence lifetimes measured at 515 and 550 nm as temperature decreases are consistent with the presence of emissive T_2 and T_1 states (Figures S25 and S26, Supporting Information). The T_2 energies, estimated from the onsets of the phosphorescence spectra of **PhCz-O-DiKTa** and **PhCz-DiKTa** at 200 K, are 2.54 and 2.51 eV (Figure S27, Supporting Information), respectively; thus, the estimated ΔE_{S1T2} values are 0.11 and 0.07 eV, respectively, which are close to predicted ΔE_{S1T2} values shown in Figure 2b. The smaller ΔE_{S1T2} of **PhCz-DiKTa** correlates with the recorded shorter τ_d and faster k_{RISC} compared to those of **PhCz-DiKTa** (Figure 5c and Table S7, Supporting Information).

2.6. OLED Performance

The thermally evaporated bottom-emitting devices with **PhCz-O-DiKTa** and **PhCz-DiKTa** were next fabricated using a device structure of ITO/HATCN (5 nm)/TAPC (40 nm)/TCTA (10 nm)/10 wt% emitter in mCP (20 nm)/TmPyPB (50 nm)/LiF (0.7 nm)/Al (100 nm) (**Figure 7**a), where ITO (indium tin oxide) serves as the transparent anode, HATCN (1,4,5,8,9,11-hexaazatriphenylene-hexacarbonitrile) acts as the hole-injection layer,

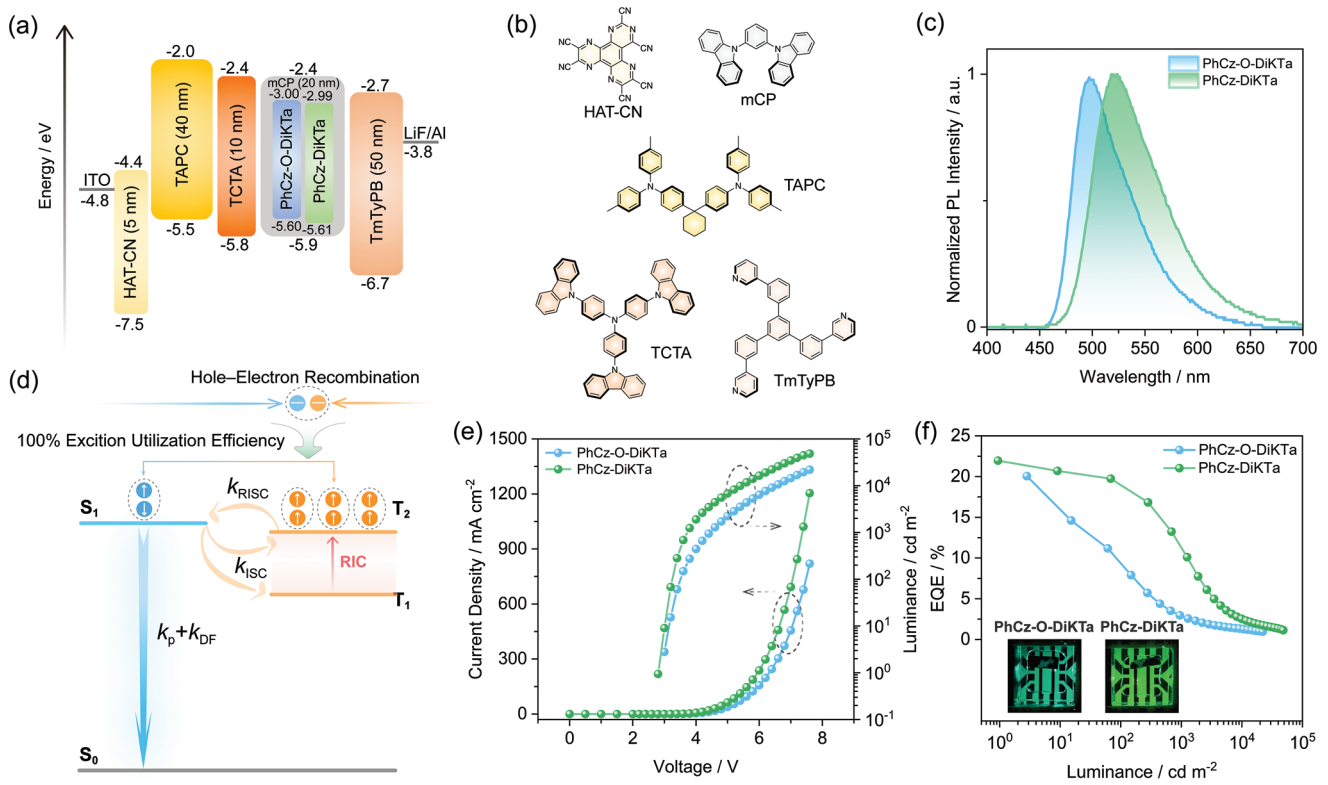

Figure 7. a) Device configuration with energy levels and thickness for each layer. b) Molecular structures of materials employed in the devices. c) EL spectra. d) Simplified Jablonski diagram showing the hole–electron recombination process under electrical excitation; RIC: reverse internal conversion. e) Current–voltage–luminance characteristic. f) EQE as a function of luminance; inset: photos of electroluminescence from the devices.

TAPC (1,1-bis[(di-4-tolylamino)phenyl]cyclohexane) act as the hole-transporting layer, TCTA act as the electron blocking layer, mCP is the host, TmPyPB (1,3,5-tris(3-pyridyl-3-phenyl) benzene) acts both as an electron transporting layer and a hole blocking layer, and LiF (lithium fluoride) acts as an electron-injection layer by modifying the work function of aluminum (Al) cathode. The molecular structures of these materials are presented in Figure 7b. Although we have demonstrated that a high doping concentration leads to emission broadening (Figure S20, Supporting Information), the 10 wt% emitter doping concentration was chosen due to the recorded high Φ_{PL} values. The EL data are summarized in **Table 1**.

Shown in Figure 7c are the EL spectra of the two devices. EL maxima (λ_{EL}) of the devices with **PhCz-O-DiKTa** and **PhCz-DiKTa** are 497 and 524 nm and associated FWHM of 58 and 72 nm, respectively. The corresponding Commission Internationale de l'Éclairage (CIE) coordinates are (0.21, 0.55) and (0.31, 0.61) (Figure S28, Supporting Information). The high coincidence in PL and EL spectra demonstrates the efficient energy transfer in the emissive layer between the host and the emitter. All the devices show relatively low turn-on voltages (V_{on}) of ≈3 eV at maximum EQE. The obtained high maximum luminance (L_{max}) is over 22 000 cd m^{-2}, benefitting from the suitable energy cascade between the functional layers (Figure 7e). Given that the measured Φ_{PL} value of **PhCz-O-DiKTa** and **PhCz-DiKTa** are 80% and 91%, respectively, the theoretical EQE_{max} values are 20% and 22.75%, assuming an out-coupling efficiency of 25%. As depicted in Figure 7f, the EQE_{max} values of the devices with **PhCz-O-DiKTa** and **PhCz-DiKTa** are 20% and 22%, reflecting that both devices reach a near 100% exciton utilization efficiency with the maximum current efficiency (CE_{max}) and power efficiency (PE_{max}) values are 56 cd A^{-1} and 58.6 lm W^{-1} of **PhCz-O-DiKTa** and 76.3 cd A^{-1} and 85.6 lm W^{-1} of **PhCz-DiKTa** devices (Figure S29, Supporting Information). However, the efficiency roll-off behavior diverges between the two devices. At a luminance of 100 cd m^{-2}, a large efficiency roll-off

Table 1. Summary of OLED performance.

Emitter	λ_{EL}[a] [nm]	FWHM[a] [nm]	CIE[a] (x, y)	V_{on}[b] [V]	CE_{max}[c] [cd A^{-1}]	PE_{max}[d] [lm W^{-1}]	EQE[e] [%]	L_{max}[f] [cd m^{-2}]
PhCz-O-DiKTa	497	58	0.21, 0.55	3	56	58.6	20/9.1/2.9	22052
PhCz-DiKTa	524	72	0.31, 0.61	2.8	76.3	85.6	22/19/11.1	48322

[a]EL maximum, FWHM, and CIE coordinates recorded at 4 V; [b]Turn-on voltage at EQE_{max}; [c]Maximum current efficiency; [d]Maximum power efficiency; [e]Maximum EQE/EQE at 100 cd m^{-2}/EQE at 1000 cd m^{-2}; [f]Maximum luminance at 7.6 V.

of 54.5% is observed in the device with **PhCz-O-DiKTa**, which is ameliorated considerably to 13.6% in the device with **PhCz-DiKTa**. The EQE reduces to 2.9% at a luminance of 1000 cd m^{-2} for the device with **PhCz-O-DiKTa**; however, for the device with **PhCz-DiKTa**, the EQE_{1000} remains at 11.1%. A plausible explanation for this difference is that the smaller ΔE_{S1T2} in **PhCz-DiKTa** serves to mitigate the efficiency roll-off due to the faster k_{RISC} and shorter delayed lifetime, thus reducing triplet exciton populations at high current densities. However, most of the previously reported ketone-based MR-TADF OLEDs showed a rather severe efficiency roll-off (>45%);[21–26,43,44] the origin of the large roll-off has not been explored in any detail. A summary of previously reported EL data related to ketone-based MR-TADF devices is presented in Figures S30 and S31, Supporting Information. This report experimentally demonstrates that the T_2 state is the key to regulating k_{RISC} (Figure 7d) and provides insight into improving the efficiency roll-off of devices, at least with ketone-containing MR-TADF derivatives.

3. Conclusions

In summary, we demonstrate how it is possible to dramatically reduce efficiency roll-off in MR-TADF OLEDs by judiciously decorating the core emitter with a **PhCz** group. This serves to reduce the ΔE_{S1T2}, leading to an accelerated RISC. Theoretical modeling of two MR-TADF emitters, **PhCz-O-DiKTa** and **PhCz-DiKTa**, predicts that the T_2 state could act as a conduit in boosting k_{RISC}. Temperature-dependent steady-state and time-gated PL measurements provided evidence of the presence and energies of the T_2 state, which explains why **PhCz-DiKTa** possesses a near 12-fold enhancement in k_{RISC} compared to **PhCz-O-DiKTa**. The OLED devices with **PhCz-O-DiKTa** and **PhCz-DiKTa** exhibited EQE_{max} values of 20% and 22%, respectively, indicating 100% exciton utilization. The remarkable divergence in efficiency roll-off of the two devices was ascribed to the smaller ΔE_{S1T2} in the device with **PhCz-DiKTa**. This study provides a rarely documented yet clear picture of the dynamics of intermediate triplet excited states and a possible solution to improve device performance without sacrificing color purity.

Supporting Information

Supporting Information is available from the Wiley Online Library or from the author.

Acknowledgements

This project received funding from the European Union's Horizon 2020 research and innovation program under the Marie Skłodowska Curie grant agreement No. 897098 (AIE-RTP-PLED). T.W. acknowledges support from the Marie Skłodowska-Curie Individual Fellowship. The authors thank the EPSRC (EP/R035164/1) for financial support.

Conflict of Interest

The authors declare no conflict of interest.

Data Availability Statement

The data that support the findings of this study are openly available in Pure (Research Information System of the University of St Andrews) at https://doi.org/10.17630/f8919b6c-4c21-4723-b862-e63aa671a014, reference number 283398031.

Keywords

conjugation modulation, emissive T_2 state, multi-resonant thermally activated delayed fluorescence, narrowband emission, organic light-emitting diodes

Received: January 15, 2023
Published online:

[1] R. Pode, *Renewable Sustainable Energy Rev.* **2020**, *133*, 110043.
[2] H. Uoyama, K. Goushi, K. Shizu, H. Nomura, C. Adachi, *Nature* **2012**, *492*, 234.
[3] Z. Yang, Z. Mao, Z. Xie, Y. Zhang, S. Liu, J. Zhao, J. Xu, Z. Chi, M. P. Aldred, *Chem. Soc. Rev.* **2017**, *46*, 915.
[4] I. S. Park, H. Komiyama, T. Yasuda, *Chem. Sci.* **2017**, *8*, 953.
[5] J. Rao, L. Yang, X. Li, L. Zhao, S. Wang, H. Tian, J. Ding, L. Wang, *Angew. Chem., Int. Ed.* **2021**, *60*, 9635.
[6] R. Ansari, W. Shao, S.-J. Yoon, J. Kim, J. Kieffer, *ACS Appl. Mater. Interfaces* **2021**, *13*, 28529.
[7] T.-Y. Cho, C.-L. Lin, C.-C. Wu, *Appl. Phys. Lett.* **2006**, *88*, 111106.
[8] T. Hatakeyama, K. Shiren, K. Nakajima, S. Nomura, S. Nakatsuka, K. Kinoshita, J. Ni, Y. Ono, T. Ikuta, *Adv. Mater.* **2016**, *28*, 2777.
[9] Y. Kondo, K. Yoshiura, S. Kitera, H. Nishi, S. Oda, H. Gotoh, Y. Sasada, M. Yanai, T. Hatakeyama, *Nat. Photonics* **2019**, *13*, 678.
[10] H. Nakanotani, T. Higuchi, T. Furukawa, K. Masui, K. Morimoto, M. Numata, H. Tanaka, Y. Sagara, T. Yasuda, C. Adachi, *Nat. Commun.* **2014**, *5*, 4016.
[11] S. O. Jeon, K. H. Lee, J. S. Kim, S.-G. Ihn, Y. S. Chung, J. W. Kim, H. Lee, S. Kim, H. Choi, J. Y. Lee, *Nat. Photonics* **2021**, *15*, 208.
[12] C.-Y. Chan, M. Tanaka, Y.-T. Lee, Y.-W. Wong, H. Nakanotani, T. Hatakeyama, C. Adachi, *Nat. Photonics* **2021**, *15*, 203.
[13] P. Jiang, J. Miao, X. Cao, H. Xia, K. Pan, T. Hua, X. Lv, Z. Huang, Y. Zou, C. Yang, *Adv. Mater.* **2022**, *34*, 2106954.
[14] Y. Zhang, D. Zhang, J. Wei, Z. Liu, Y. Lu, L. Duan, *Angew. Chem., Int. Ed.* **2019**, *58*, 16912.
[15] X. Cai, J. Xue, C. Li, B. Liang, A. Ying, Y. Tan, S. Gong, Y. Wang, *Angew. Chem., Int. Ed.* **2022**, *134*, e202200337.
[16] M. Yang, I. S. Park, T. Yasuda, *J. Am. Chem. Soc.* **2020**, *142*, 19468.
[17] F. Liu, Z. Cheng, Y. Jiang, L. Gao, H. Liu, H. Liu, Z. Feng, P. Lu, W. Yang, *Angew. Chem., Int. Ed.* **2022**, *61*, e202116927.
[18] Y. Liu, X. Xiao, Z. Huang, D. Yang, D. Ma, J. Liu, B. Lei, Z. Bin, J. You, *Angew. Chem., Int. Ed.* **2022**, *61*, e202210210.
[19] X. Wu, B.-K. Su, D.-G. Chen, D. Liu, C.-C. Wu, Z.-X. Huang, T.-C. Lin, C.-H. Wu, M. Zhu, E. Y. Li, W.-Y. Hung, W. Zhu, P.-T. Chou, *Nat. Photonics* **2021**, *15*, 780.
[20] D. Hall, S. M. Suresh, P. L. dos Santos, E. Duda, S. Bagnich, A. Pershin, P. Rajamalli, D. B. Cordes, A. M. Slawin, D. Beljonne, *Adv. Opt. Mater.* **2020**, *8*, 1901627.
[21] Y. Yuan, X. Tang, X. Y. Du, Y. Hu, Y. J. Yu, Z. Q. Jiang, L. S. Liao, S. T. Lee, *Adv. Opt. Mater.* **2019**, *7*, 1801536.
[22] D. Sun, S. M. Suresh, D. Hall, M. Zhang, C. Si, D. B. Cordes, A. M. Slawin, Y. Olivier, X. Zhang, E. Zysman-Colman, *Mater. Chem. Front.* **2020**, *4*, 2018.
[23] X. Li, Y.-Z. Shi, K. Wang, M. Zhang, C.-J. Zheng, D.-M. Sun, G.-L. Dai, X.-C. Fan, D.-Q. Wang, W. Liu, Y.-Q. Li, J. Yu, X.-M. Ou,

C. Adachi, X.-H. Zhang, *ACS Appl. Mater. Interfaces* **2019**, *11*, 13472.
[24] S.-N. Zou, C.-C. Peng, S.-Y. Yang, Y.-K. Qu, Y.-J. Yu, X. Chen, Z.-Q. Jiang, L.-S. Liao, *Org. Lett.* **2021**, *23*, 958.
[25] D. Hall, S. M. Suresh, P. L. dos Santos, E. Duda, S. Bagnich, A. Pershin, P. Rajamalli, D. B. Cordes, A. M. Z. Slawin, D. Beljonne, A. Köhler, I. D. W. Samuel, Y. Olivier, E. Zysman-Colman, *Adv. Opt. Mater.* **2020**, *8*, 1901627.
[26] S. Wu, W. Li, K. Yoshida, D. Hall, S. M. Suresh, T. Sayner, J. Gong, D. Beljonne, Y. Olivier, I. D. W. Samuel, E. Zysman-Colman, *ACS Appl. Mater. Interfaces* **2022**, *14*, 22341.
[27] F. Huang, K. Wang, Y.-Z. Shi, X.-C. Fan, X. Zhang, J. Yu, C.-S. Lee, X.-H. Zhang, *ACS Appl. Mater. Interfaces* **2021**, *13*, 36089.
[28] M. K. Etherington, J. Gibson, H. F. Higginbotham, T. J. Penfold, A. P. Monkman, *Nat. Commun.* **2016**, *7*, 13680.
[29] B. H. Drummond, N. Aizawa, Y. Zhang, W. K. Myers, Y. Xiong, M. W. Cooper, S. Barlow, Q. Gu, L. R. Weiss, A. J. Gillett, D. Credgington, Y.-J. Pu, S. R. Marder, E. W. Evans, *Nat. Commun.* **2021**, *12*, 4532.
[30] T. Wang, J. De, S. Wu, A. K. Gupta, E. Zysman-Colman, *Angew. Chem., Int. Ed.* **2022**, *61*, e202206681.
[31] T. Wang, A. K. Gupta, S. Wu, A. M. Z. Slawin, E. Zysman-Colman, *J. Am. Chem. Soc.* **2023**, *145*, 1945.
[32] C. Adamo, V. Barone, *J. Chem. Phys.* **1999**, *110*, 6158.
[33] G. A. Petersson, T. G. Tensfeldt, J. A. Montgomery Jr., *J. Chem. Phys.* **1991**, *94*, 6091.
[34] S. Hirata, M. Head-Gordon, *Chem. Phys. Lett.* **1999**, *314*, 291.
[35] D. Hall, J. C. Sancho-García, A. Pershin, G. Ricci, D. Beljonne, E. Zysman-Colman, Y. Olivier, *J. Chem. Theory Comput.* **2022**, *18*, 4903.
[36] A. Pershin, D. Hall, V. Lemaur, J.-C. Sancho-Garcia, L. Muccioli, E. Zysman-Colman, D. Beljonne, Y. Olivier, *Nat. Commun.* **2019**, *10*, 597.
[37] R. A. Kendall, T. H. Dunning Jr, R. J. Harrison, *J. Chem. Phys.* **1992**, *96*, 6796.
[38] N. G. Connelly, W. E. Geiger, *Chem. Rev.* **1996**, *96*, 877.
[39] T. Lu, F. Chen, *J. Comput. Chem.* **2012**, *33*, 580.
[40] D. Zhang, M. Cai, Z. Bin, Y. Zhang, D. Zhang, L. Duan, *Chem. Sci.* **2016**, *7*, 3355.
[41] M. Kasha, H. R. Rawls, M. A. El-Bayoumi, *Pure Appl. Chem.* **1965**, *11*, 371.
[42] R. A. Marcus, *J. Chem. Phys.* **1956**, *24*, 966.
[43] J.-F. Liu, S.-N. Zou, X. Chen, S.-Y. Yang, Y.-J. Yu, M.-K. Fung, Z.-Q. Jiang, L.-S. Liao, *Mater. Chem. Front.* **2022**, *6*, 966.
[44] S. Wu, A. K. Gupta, K. Yoshida, J. Gong, D. Hall, D. B. Cordes, A. M. Z. Slawin, I. D. W. Samuel, E. Zysman-Colman, *Angew. Chem., Int. Ed.* **2022**, *61*, e202213697.